

SCIENTIFIC REPORTS



OPEN

Exotic skyrmion crystals in chiral magnets with compass anisotropy

J. P. Chen^{1,2}, Dan-Wei Zhang³ & J. -M. Liu^{1,4}

Received: 27 January 2016

Accepted: 15 June 2016

Published: 05 July 2016

The compass-type anisotropy appears naturally in diverse physical contexts with strong spin-orbit coupling (SOC) such as transition metal oxides and cold atomic gases etc, and it has been receiving substantial attention. Motivated by recent studies and particularly recent experimental observations on helimagnet MnGe, we investigate the critical roles of this compass-type anisotropy in modulating various spin textures of chiral magnets with strong SOC, by Monte Carlo simulations based on a classical Heisenberg spin model with Dzyaloshinsky-Moriya interaction and compass anisotropy. A phase diagram with emergent spin orders in the space of compass anisotropy and out-of-plane magnetic field is presented. In this phase diagram, we propose that a hybrid super-crystal structure consisting of alternating half-skyrmion and half-anti-skyrmion is the possible zero-field ground state of MnGe. The simulated evolution of the spin structure driven by magnetic field is in good accordance with experimental observations on MnGe. Therefore, this Heisenberg spin model successfully captures the main physics responsible for the magnetic structures in MnGe, and the present work may also be instructive to research on the magnetic states in other systems with strong SOC.

Spin-orbit coupling (SOC) plays an important role in condensed matter physics, especially in recently addressed quantum spin Hall effects and related topological orders^{1,2}. So far, magnetic materials with lacking inversion symmetry in B20 cubic crystal structure provide an alternative arena for studying the emergent phenomena in magnets of strong SOC. Prominent members encompass metallic compounds like MnSi³⁻⁵ and FeGe⁶, semiconductor Fe_{1-x}Co_xSi^{7,8}, and multiferroic insulator Cu₂OSeO₃⁹. In these materials, the competitions between strong ferromagnetic (FM) exchanges, weak Dzyaloshinsky-Moriya (DM) interactions, and additional magnetic anisotropies originating from high-order interactions, generate a long-wavelength helical spin order which propagates along some specific directions favored by these magnetic anisotropies³⁻⁵.

The roles of magnetic anisotropies are usually delicate but substantial in determining the magnetic ground states in some cases. Generally, these anisotropy terms are the weakest in energy scale among the above mentioned interactions, and the favored directions of helical spin orders are materials-dependent. For example, the helical order in MnSi observed in neutron scattering experiments is characterized by a set of Bragg peaks situated on a sphere surface, suggesting that the spin alignment of the helical state is locked along the cubic space diagonal $\langle 111 \rangle$ directions, due to the effect of high-order crystal anisotropies³⁻⁵. On the other hand, a perpendicular external magnetic field may transform the single twisted helice to the energetically favorable hexagonal skyrmion crystal (SkX) structure^{4,8}. This intriguing topological structure has been receiving tremendous interest due to its unusual magnetic and transport properties, especially the topological Hall effect¹⁰⁻¹².

Nevertheless, recent experiments on B20-type cubic MnGe^{11,13} revealed the field dependence of the topological Hall effect which is distinct from those observed in other B20-type compounds, suggesting a zero-field ground state skyrmion lattice very different from often observed hexagonal SkX. So far, no recognized theory for this unusual skyrmion lattice is available. In addition, the helical wavelength λ changes from 3 nm to 6 nm with temperature, which is much smaller than that in conventional B20-type compounds with typical λ of 18–90 nm. Therefore, a different mechanism for the spin structure in this generic B20 MnGe is expected. One possible interpretation of the variation in small-angle neutron scattering (SANS) patterns with magnetic field is the presence of an easy axis of magnetization along the $\langle 100 \rangle$ direction¹³. This implies that MnGe may have strong SOC and

¹Laboratory of Solid State Microstructures and Innovative Center of Advanced Microstructures, Nanjing University, Nanjing 210093, China. ²School of Physics and Electronic Engineering, Guangzhou University, Guangzhou 510006, China. ³Guangdong Provincial Key Laboratory of Quantum Engineering and Quantum Materials, SPTE, South China Normal University, Guangzhou 510006, China. ⁴Institute for Advanced Materials, South China Normal University, Guangzhou 510006, China. Correspondence and requests for materials should be addressed to J.P.C. (email: chankaipei@163.com)

consequent non-negligible and high-order magnetic anisotropy due to SOC, so that the modulation vector \mathbf{q} is locked along the $\langle 100 \rangle$ direction. In this sense, the appearance of exotic skyrmion state is easy to understand.

Another scenario for the existence of high-order anisotropy terms in B20-type transition-metal silicides and germanides is associated with the weak itinerant-electron ferromagnetism¹⁴. The outermost electrons in these compounds can be described by an extended Hubbard model on the two-dimensional (2D) lattice. The Hamiltonian consists of the nearest-neighbor natural hopping (t_0), SOC-induced hopping (t_{SO}), and Hubbard repulsion (U)^{15–18}:

$$\mathcal{H} = -t_0 \sum_{\langle i,j \rangle, \sigma} c_{i,\sigma}^+ c_{j,\sigma} - t_{SO} \sum_{i,\eta,\alpha,\beta} (c_{i,\alpha}^+ \sigma_{\alpha,\beta}^\eta c_{i+\hat{\eta},\beta} + h.c.) + U \sum_i n_{i\uparrow} n_{i\downarrow}, \quad (1)$$

where $c_{i,\sigma}^+$ is the operator creating a spin- σ ($\sigma = \uparrow, \downarrow$) electron at site i , and $\sigma_{\alpha,\beta}^\eta$ denotes the elements of the Pauli matrix with superscript $\eta = x, y$. In the large U condition, one can obtain an effective spin Hamiltonian, by a combination of the Heisenberg exchange (J), DM interaction (D), and quantum compass anisotropy (A_c)^{15–19}:

$$\begin{aligned} \mathcal{H} &= -J \sum_i \mathbf{S}_i \cdot (\mathbf{S}_{i+\hat{x}} + \mathbf{S}_{i+\hat{y}}) - D \sum_i (\mathbf{S}_i \times \mathbf{S}_{i+\hat{x}} \cdot \hat{x} + \mathbf{S}_i \times \mathbf{S}_{i+\hat{y}} \cdot \hat{y}) \\ &\quad - A_c \sum_i (S_i^x S_{i+\hat{x}}^x + S_i^y S_{i+\hat{y}}^y) \\ S_i^\mu &= \frac{1}{2} \sum_{\alpha,\beta} c_{i,\alpha}^+ \sigma_{\alpha,\beta}^\mu c_{i,\beta} \end{aligned} \quad (2)$$

where S_i^μ is the spin vector with $\mu \equiv (x, y, z)$. By defining $t = (t_0^2 + t_{SO}^2)^{1/2}$, $\tan\theta = t_{SO}/t_0$, and $J_0 = 4t^2/U$, one can obtain $J = J_0 \cdot \cos 2\theta$, $D = J_0 \cdot \sin 2\theta$, and $A_c = J_0 \cdot (1 - \cos 2\theta)$ ¹⁶. For magnetic systems with strong SOC, an easy-plane anisotropy term, i.e. the so-called “compass anisotropy ($A_c > 0$)”, appears naturally^{15,16}. This Hamiltonian has recently been used to deal with ultra-cold atoms with artificial SOC on a 2D optical lattice or three-dimensional (3D) counterpart^{17,18}.

In fact, in the context of solid state physics, hybrid models interpolating between Heisenberg models and compass models are often proposed^{20–23}. Such hybrid models resulting from Hubbard models are relevant to describe the superexchange interactions in transition metal systems with strong SOC, such as those containing 4d and 5d ions Rh, Ru, Os, and Ir, where the effective moments carry both the orbital and spin characters^{20,22,23}. An example can be found in recent experiments demonstrating the coexistence of superconductivity and ferromagnetism on the interfaces between LaAlO₃ and SrTiO₃ (2D electron gas)²⁴. Interestingly, relevant magneto-transport studies show a strong and gate-tunable Rashba SOC for these 2D conduction electrons, arising from the broken inversion symmetry at the interface²⁵. Subsequently, the microscopic mechanism for the interfacial magnetism using a microscopic model (derived from an extended Hubbard model with Rashba SOC) was investigated^{15,16}. Both the numerical and analytical calculations predict a long-wavelength spiral ground state with a SOC-dependent pitch under zero magnetic field, while hedgehog-like skyrmions appear over a broad range of magnetic field. While the relevant mechanisms for these emergent phenomena have been disputed, the possible role of the compass anisotropy thus becomes interested to some extent^{15–18,20,22}.

From the viewpoint of energy scale, the compass anisotropy is usually ignored in the literature, since it is an even higher order than the DM term which is already insignificant. We discuss this exceptional issue from several levels:

(1) First, considering a chiral magnet with commonly weak SOC ($t_{SO}/t_0 \ll 1$), the contribution of compass anisotropy term to the total energy is on an order of magnitude of $A_c \sim J \cdot (t_{SO}/t_0)^2$ which is much smaller than the DM term $D \sim J \cdot (t_{SO}/t_0) \ll J$ ¹⁶. However, MnGe has strong SOC and this compass anisotropy term can no longer be trivial and must be taken into account, for its contribution to the energy is comparable to the DM term ($\sim D^2/J$)^{15,16}.

(2) Second, the effect of uniaxial anisotropy $A_s(S_i^z)^2$ on the helical state and SkX in B20-type helimagnets was once studied²⁶. In phenomenological sense, this uniaxial anisotropy arises from the single-ion or dipolar shape anisotropy, and thus can be either an easy-axis ($A_s < 0$) or hard-axis ($A_s > 0$) anisotropy²⁷. To this stage, the effective anisotropy in these materials is governed by $A = A_c + A_s$. In some cases, the uniaxial anisotropy is vanished or much smaller than the compass term, which is typically true in MnGe and those magnetic systems with strong SOC mentioned above^{15,16}. This implies that the compass anisotropy can be a dominant ingredient in the effective anisotropy term in these cases, which has not been well recognized earlier^{11,13,15,16}.

(3) Third, it is noted that the anisotropy ingredients would possibly be sensitive to external stimuli. While the uniaxial anisotropy can be tuned by strain²⁷, the compass anisotropy may be modulated largely too by external stimuli (e.g. external electric field), as motivated by the tunable SOC in 2D electron gas systems^{28,29}. These allow possibilities to explore the spin states in chiral magnets with tunable A (either uniaxial or compass or both). Obviously, along the line supported by the above three-level discussion, one has sufficient reasons for a theoretical study on the helimagnets with compass anisotropy like MnGe.

In this work, we investigate the spin ground states in such chiral magnets with multifold interactions, using Monte Carlo (MC) simulation³⁰. Specific attention is paid to the roles of the compass anisotropy. We first explore the phase diagram in the (H_z, A) -space, which demonstrates the roles of the compass anisotropy in modulating the spin states. Then, we suggest an intriguing alternating half-skyrmion (Hsk) and half-anti-skyrmion (HASK) crystal structure (i.e., a state in the phase diagram) to be a candidate for the zero-field ground state of MnGe compound, confirmed by the quite good qualitative consistence of the MC simulations with experiments. We believe that this study provides a theoretical guide to understand the magnetic structures and their evolutions in those helimagnets with strong SOC.

Results

Model and Simulation. Considering the helical and skyrmion spin structures in helimagnets MnGe, MnSi, Fe_{1-x}Co_xSi etc, it does not lose a generality to start from a 2D $L \times L$ square lattice with periodic boundary conditions. One Heisenberg spin S_i is imposed on each site i . The Heisenberg exchange interactions, DM interactions, compass anisotropy terms, and Zeeman term are considered. The Hamiltonian Eq. (2) is thus re-written as:

$$\begin{aligned} \mathcal{H} = & -J \sum_i S_i \cdot (S_{i+\hat{x}} + S_{i+\hat{y}}) - D \sum_i (S_i \times S_{i+\hat{x}} \cdot \hat{x} + S_i \times S_{i+\hat{y}} \cdot \hat{y}) \\ & - A \sum_i (S_i^x S_{i+\hat{x}}^x + S_i^y S_{i+\hat{y}}^y) - H \cdot \sum_i S_i, \end{aligned} \quad (3)$$

where field H is along the z -axis or $-x$ -axis or stated elsewhere. The uniaxial anisotropy favors the hard-axis along the z -axis at $A_s > 0$, or the easy-axis along the z -axis at $A_s < 0$. Here, A_s is a minor quantity in comparison with A_c . In this sense, one may reckon that the synthetic anisotropy term (A) still prefers the in-planar 90° compass-type symmetry. We will simply treat this synthetic easy-plane anisotropy as the compass anisotropy hereafter.

In the classical approximation, we treat spins S_i as classical vectors and aim at minimizing the energy for finding the ground-state spin configurations $\{S_i\}$. It is noted that the classical MC simulation has been used to explore the phase diagrams of effective spin models in the similar context, e.g. chiral magnets^{8,31}, and even ultra-cold atomic systems^{17,18}. Therefore, we restrict our discussion on the classical approximations, while a full quantum treatment would be needed to have a deeper understanding of quantum spin models, which is beyond the present work.

For simplicity, we use dimensionless units for convenience: spatial length is scaled by the lattice spacing a . Parameters D , A , and H are quantified in the units of J/a , J , $J \cdot S$, respectively. The spin moment $S \equiv 1$ and $a = 1$ are taken without loss of generality. In this case, the spin phase texture is determined by ratios between D , A , and H . In the simulation, we choose ratio $D/J = \sqrt{6}$, yielding the helical wavelength $\lambda \sim 8a$ for the spin structure in MnGe. Note that the typical helical wavelength λ is ~ 4.0 nm for MnGe, and the lattice constant a is ~ 0.48 nm³², which is on the same order of magnitude as that of the helical states obtained in our simulations. The simulation algorithm and details of the calculation procedure are presented in the Method section below.

The as-simulated spin structures are characterized by several physical quantities, as suggested in literature³¹. First, the spatial symmetry of spin structure is reflected in the Bragg intensity pattern $|S(q)|^2$, with reciprocal momentum $S(q)$ obtained from the Fourier transformation of the spin configuration:

$$S(q) = \frac{1}{N} \sum_i S_i \exp(-iq \cdot r_i), \quad (4)$$

where $N = L^2$ is the total number of spins and r_i is the spatial coordinate.

To characterize swirling structure of the skyrmions lying on the xy -plane, we introduce the local density of skyrmions χ_i at lattice site i , defined as:

$$\chi_i = \frac{1}{8\pi} [S_i \cdot (S_{i+\hat{x}} \times S_{i+\hat{y}}) + S_i \cdot (S_{i-\hat{x}} \times S_{i-\hat{y}})], \quad (5)$$

which is the discretization counterpart of the skyrmion density $S \cdot (\partial_x S \times \partial_y S) / 4\pi$ for the continuum case⁴. The summation of χ_i over the extended coordinate space gives the so-called topological winding number (skyrmion number) as $\chi = \sum_i \chi_i$, which is proportional to the topological Hall resistivity ρ_{yx}^T . One single skyrmion cell contributes one unit to χ in the continuum limit.

The helicity of a skyrmion state or a helical state is closely related to the spin chirality via the relativistic SOC. We define the helicity as³³:

$$\gamma = \frac{1}{N} \sum_i S_i \times S_{i+\hat{x}} \cdot \hat{x} + S_i \times S_{i+\hat{y}} \cdot \hat{y}, \quad (6)$$

where the sign and magnitude of γ reflect respectively the spin swirling direction (i.e., left or right handedness) and degree of swirl in a proper screw spin structure.

Moreover, we define the out-of-plane magnetization, in-plane magnetization, and total magnetization, respectively as:

$$\begin{aligned} \langle M_z \rangle & \equiv \frac{1}{N} \sum_i \langle S_i^z \rangle \\ \langle M_{xy} \rangle & \equiv \sqrt{\langle M_x \rangle^2 + \langle M_y \rangle^2}, \quad \langle M_{x,y} \rangle \equiv \frac{1}{N} \sum_i \langle S_i^{x,y} \rangle \\ \langle M_{xyz} \rangle & \equiv \sqrt{\langle M_x \rangle^2 + \langle M_y \rangle^2 + \langle M_z \rangle^2}, \end{aligned} \quad (7)$$

where $\langle \dots \rangle$ refers to the thermal and configuration averaging at a given temperature T .

Low temperature phase diagram. Extensive simulations over a broad region on the (A, H_z) plane generate a low temperature phase diagram, as summarized in Fig. 1. Here H_z denotes the field H along the z -axis. Some typical spin structures of these phases are presented in Fig. 2. To illustrate the spin configurations, we use the color

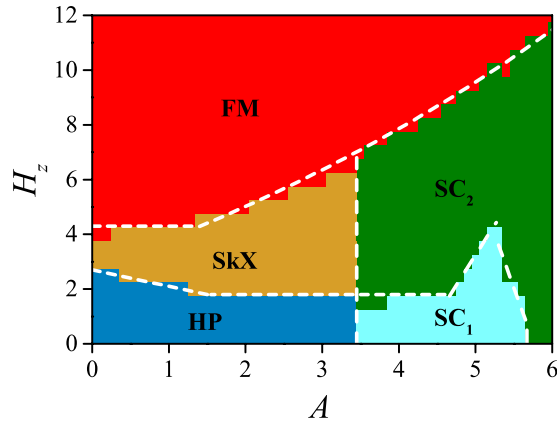


Figure 1. Low temperature ($T=0.01$) phase diagram of the spin model in Eq. (3) with $D=\sqrt{6}J$, and H along the z -axis (H_z). Spin configurations are abbreviated as SkX (skyrmion crystal), HP (helical phase), SC (spin crystal), and FM (ferromagnetic) phase. Two types of spin crystals are identified as SC_1 and SC_2 according to their different symmetry. Phase boundaries are marked by white dashed lines.

map to scale the spin components along the z -axis (out-of-plane) S_i^z , and use the spin vectors (arrows) to describe the on-plane xy components S_i^{xy} .

For very low $H_z \sim 0$ in Fig. 1, the result shows the spin structure transition from helical phases (HP) to spin crystal (SC) phases, as the anisotropy A increases from zero. Upon applying of an intermediate H_z , the HP and SC_1 phase evolve respectively into the SkX phase and SC_2 phase, as shown in Fig. 2(b,d). At high H_z , the lattice gradually gives away to the FM phase, with all spins orientating along the z -axis. This phase transition sequence is consistent with the one in previous studies³¹.

In Fig. 2(c,d), one may find from the Bragg patterns that these crystal structures are constructed primarily from the superimposition of two helices, one oriented along the x -axis and the other along the y -axis, as characterized by two pairs of Bragg peaks. Here, the equality of these two pairs of Bragg intensities can be used as a criterion to classify the chiral crystal states: the SC_1 phase (unequal intensities) and SC_2 phase (equal intensities), following earlier studies³¹. Therefore, the increasing compass anisotropy leads to the transformation from single- q spin structures (i.e. HP) to double- q spin structures (i.e. SC phases). In the following of this work, we emphasize in the SC phases and investigate their topological properties and magnetic-field-induced evolution behaviors.

The SC_2 phase: candidate for the ground state of MnGe. Now we investigate the spin crystal phases, i.e. the SC_1 and SC_2 phases shown in Fig. 2(c,d). These spin crystal phases were proposed theoretically³⁴, and they have been confirmed by the recent experimental observations on MnGe^{11,13}. The neutron scattering revealed the multiple- q helix structure in MnGe in response to increasing H , with the spin helix q vectors locked along the $\langle 100 \rangle$ direction due to an additional anisotropy originating from the SOC. More importantly, given a square or cubic SkX structure, the Berry phase calculations fit quite well the observed H -dependent topological Hall resistivity. In contrast, if a hexagonal SkX structure in MnSi and $Fe_{1-x}Co_xSi$ is assumed, the calculations fail to fit the observed topological Hall resistivity as a function of H . Therefore, the MnGe most likely prefers the square or cubic SkX structures rather than a hexagonal SkX structure¹³.

The square SkX structure or the 2D counterpart of cubic SkX structure is just the SC_2 phase presented in Fig. 2(d). However, knowledge on microscopic mechanism for the possible SC_2 phase in MnGe is still lacking¹³. The present work proposes that it is just the compass anisotropy originating from the SOC responsible for formation of the SC phases, noting again that MnGe has strong SOC. To proceed, we start from a SC structure on a 2D plane, which can be viewed as a superimposition of two single helical states³⁴:

$$S(x, y) = I[C_1(\sin(qy), 0, B\cos(qy)) + C_2(0, \cos(qx), B\sin(qx))] \\ I \equiv I(x, y) = \frac{1}{\sqrt{(C_1\sin qy)^2 + (C_2\cos qx)^2 + B^2(C_1\cos qy + C_2\sin qx)^2}} \quad (8)$$

where $I \equiv I(x, y)$ is a normalized factor, B ($0 < B \leq 1$) is a variable associated with the compass anisotropy term A , which stands for the compression of the helical ordering along the z -axis brought about by the easy-plane compass anisotropy term. C_1 and C_2 represent the specific weight of the two helices, as characterized by the relative intensities of the two pairs of the Bragg spots shown in Fig. 2(c,d).

The SC_1 and SC_2 phases as the ground states at $H=0$. We first study the spin structures and possible topological properties of the SC_1 and SC_2 phases under $H=0$, corresponding to the Eq. (8) with $C_1 \neq C_2$ and $C_1 = C_2$, respectively. The typical spin configurations of the two phases are plotted in Fig. 3(a,b) respectively. While the SC_1 phase is relatively trivial, we concentrate on the SC_2 phase. We find a periodic array of “nodes” (magnetization nodes) in the SC_2 phase, where the spin vector $S_i = 0$ ³⁵. These singular points can be easily seen from Eq. (8) if one sets $(\sin qx = 1, \cos qy = -1)$ or $(\sin qx = -1, \cos qy = 1)$. The hard-spin constraint $|S_i| = 1$ are

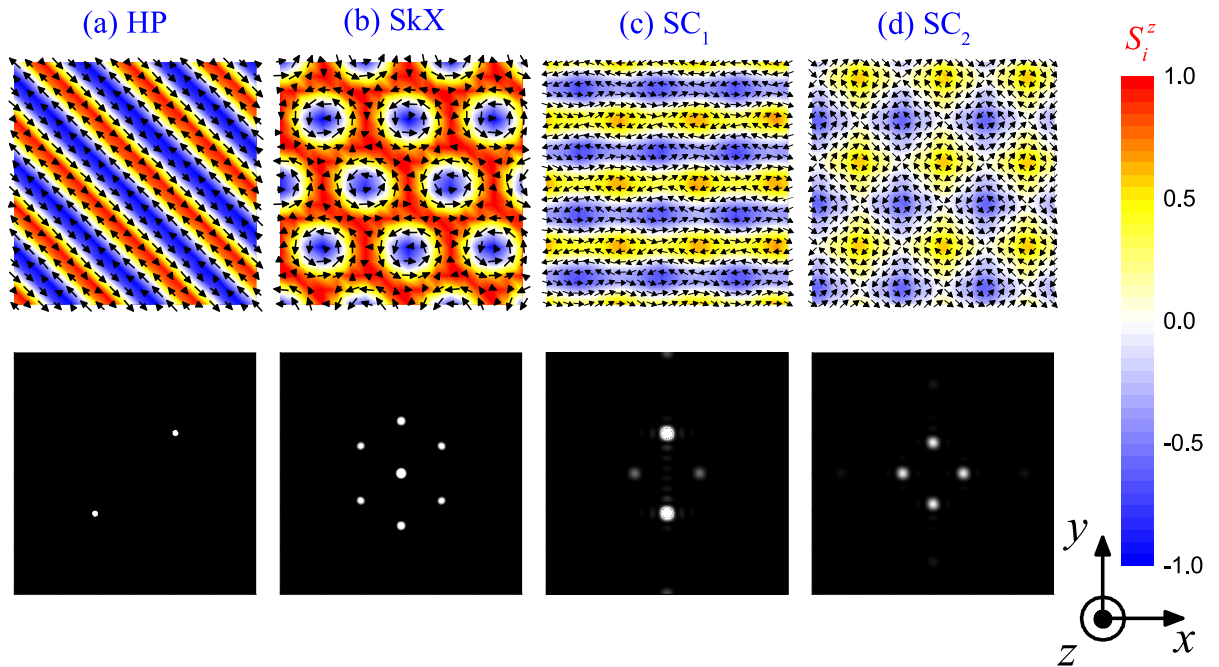


Figure 2. Plot of some typical spin configurations arising in the phase diagram (Fig. 1): (a) HP state at $(A, H_z) = (0.2, 0.0)$, (b) SkX phase at $(A, H_z) = (0.2, 2.6)$, (c) SC_1 phase at $(A, H_z) = (4.2, 0.0)$ and (d) SC_2 phase at $(A, H_z) = (6.0, 0.0)$, with the corresponding Bragg intensity $|S(q)|^2$ patterns shown at the bottom.

used in the simulation, where the singularities are naturally forbidden. In fact, however, it is possible that the spins in real chiral magnets are soft due to their interactions with the metallic host or the averaging over fast fluctuations, leading to the possible points of vanishing magnetization. The electronic structure of this nodal topological lattice had been studied recently³⁶. However, we find that the magnetic nodes don't impose substantial impact on the field dependent behaviors and topological properties of the SC_2 phase, and here we no longer give more discussion on the nodes. The SC_2 phase consists of alternative alignment of two square flux units, with two specific units enclosed by the dash lines in Fig. 3(b). We calculate the topological winding number χ of such two units by adopting a numerical procedure. First, the 2D lattice is discretized on a square mesh with grids up to $N \times N$, and then the χ_i at each grid point is calculated using Eq. (5). Second, all the χ_i over the defined region are summed, where an enough big N is taken so that the error is on the order of $\mathcal{O}(4\pi^2/N^2)$ ³⁷.

The numerical results show $\chi = 1/2$ for one flux unit, and $\chi = -1/2$ for another one. Note that the calculated results don't depend on factor B within $0.0 < B \leq 1.0$. The topological winding number $\chi = 1/2$ or $-1/2$ for the square flux indicate that this unit is a half-anti-skyrmion (HASK) structure or a half-skyrmion (Hsk) structure, with the schematic spin configurations shown in Fig. 3(c,d), respectively. Therefore, the SC_2 phase at $H \sim 0$ is a spin crystal structure consisting of alternating Hsk and HASK units.

It is known that a skyrmion can be topologically mapped into a hairy sphere (or a hedgehog). The vortex-like skyrmion texture found in MnSi and $Fe_{1-x}Co_xSi$ is topologically equivalent to such a hairy sphere³⁸. Applying this topology property to the SC_2 phase here, one may unfold the Hsk and HASK units and map them respectively onto the upper hemisphere and lower hemisphere of the hairy sphere, as shown in Fig. 3(c)–(f). In the other words, the Hsk and HASK units can be obtained from splitting a skyrmion into two halves. In this sense, the compass anisotropy causes the fractionalization of the skyrmions.

Evolution of the SC_2 phase in response to H_z . Subsequently, we investigate the evolution of the SC_2 phase in response to the cycling of H . To compare with experiments^{11,13}, we focus on the cases of H along the z -axis (H_z) and $-x$ -axis (H_{-x}). All the simulations start from the initial lattice which is equilibrated at $H = 0$, $D = \sqrt{6}$, $A = 6.0$, and $T = 0.01$, corresponding to the zero-field cooling in experiments. A series of parameters characterizing the SC_2 phase in response to increasing H_z are plotted in Fig. 4. Here the H_z is varying gradually from zero to a value big enough for saturating the FM phase and then back to zero.

We first look at the evolutions in the H_z -increasing half loop. Figure 4(a) shows that the thermal-averaged $\langle \chi \rangle$ gradually drops from zero to a negative maximal of -5.0 at $H_z = 5.5$, implying a broken balance of the χ -contributions from the Hsk and HASK units in the SC_2 phase. In the simulation, it is found that the positive skyrmion density in the Hsk units reduces markedly, leading to a negative net spin chirality, with the spin structure at $H_z = 5.5$ shown in Fig. 4(g). Further increasing of H_z drives the $\langle \chi \rangle$ back and eventually to die away at $H_z \sim 12.0$ (corresponding to the FM state). The evolution from the SC_2 phase to the FM state is not always continuous, but featured with a sharp jump in the $\langle \chi \rangle$ - H_z curve at $H_z \sim 10.3$, accompanied with an abrupt expansion of the HASK unit size and also abrupt jump of the SC periodicity. The spin structures right below and above this jump point are presented in Fig. 4(h,i). Similar phenomenon was also observed in the melting of hexagonal SkX

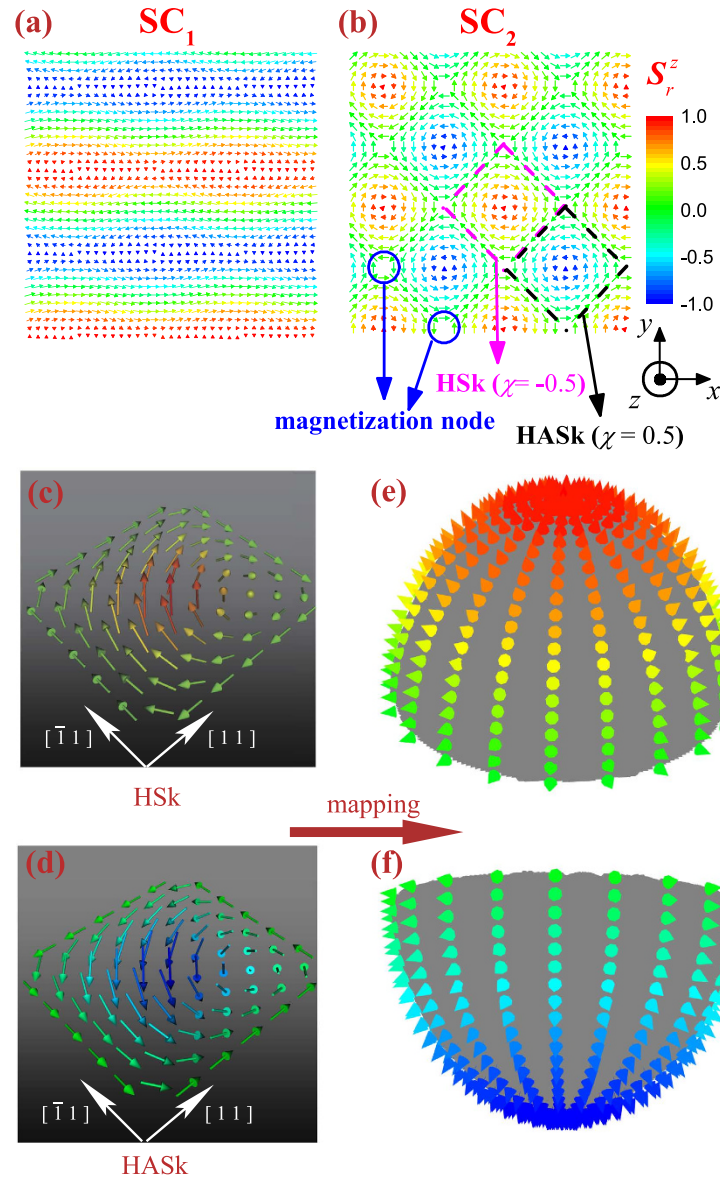


Figure 3. Plots of (a) SC_1 structure given by the expression Eq. (8) with specific parameters $q = 2\pi/30$, $C_1 = 0.8$, $C_2 = 0.2$, and $B = 0.9$; and (b) SC_2 structure with $B = 0.5$, where we find the profile of plotted SC_2 state with the parameter $B = 0.5$ gives a good fit with that obtained from the MC simulation. A primitive cell in the SC_2 structure is composed by a HSk structure and a HASK structure, which are enclosed by the dark and pink dash lines, respectively. (c,d) Schematic illustrations of the spin configurations in a HSk and a HASK structure in the SC_2 structure, respectively. (e,f) Schematic mapping from a HSk or a HASK spin structure to a hemisphere of the hairy sphere.

structure. In this process, the increasing H_z destroys the thermal-averaged helicity $\langle \gamma \rangle$ of the SC_2 phase, as seen clearly by the $\langle \gamma \rangle - H_z$ curves shown in Fig. 4(b).

Then we look at the H_z -decreasing half loop. Different from the H_z -increasing half loop, the lattice returns back to a spin structure aligned along the $\langle 10 \rangle$ direction rather than the SC_2 phase, as shown in Fig. 4(j). This spin structure is characterized by a zigzag pattern with striped domain of alternating M_z . The simulations on an extended 64×64 lattices confirm the existence of the zigzag striped domains. It is noted that no thermal hysteresis effect appearing in the evolution of magnetic state during the process of increasing and decreasing the magnetic field, as shown by the simulated $\langle E \rangle - H_z$ loop in Fig. 4(c). Therefore, the different magnetic states emerging during this evolution sequence suggest that these states are basically degenerate. Typically, the zigzag striped domains and the SC_2 phase at $H_z = 0$ have the same energy. The zigzag spin pattern may align along one of $\langle 10 \rangle$ directions on the xy -plane at random. Considering the zigzag-patterned spin structure which aligns along the y -axis shown in Fig. 4(j), the average x component $\langle M_x \rangle$ of magnetization is ~ 0 , leaving the nonzero $\langle M_y \rangle$. However, the values of $\langle M_x \rangle$ and $\langle M_y \rangle$ reverse for the zigzag pattern aligned along the x -axis. Therefore, we use in-plane magnetization $\langle M_{xy} \rangle$ rather than $\langle M_x \rangle$ and $\langle M_z \rangle$ to characterize the formation of zigzag-patterned

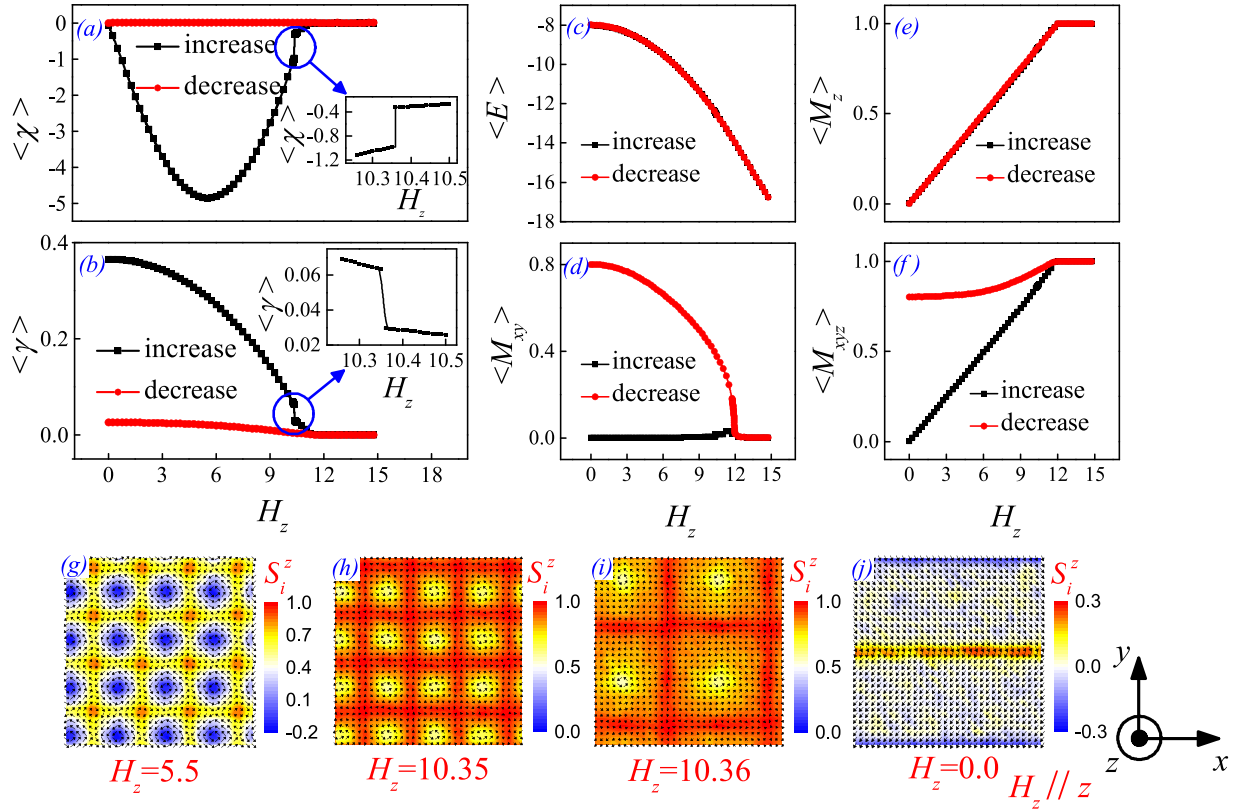


Figure 4. Plots of various physical quantities as a function of H_z : (a) $\langle \chi \rangle$, (b) $\langle \gamma \rangle$, (c) thermal-averaged energy per spin $\langle E \rangle$, (d) $\langle M_{xy} \rangle$, (e) $\langle M_z \rangle$, and (f) $\langle M_{xyz} \rangle$. Here $\langle \chi \rangle$ denotes the thermal average of skyrmion number counted on the spin lattice, and $\langle \gamma \rangle$ denotes thermal average of the helicity per spin. In this process, spin configurations evolve from the initial SC₂ state at $H = 0$ to a saturated FM phase driven by the increasing H_z , with the state carrying the negative maximal value of χ at $H_z = 5.5$ shown in (g). Also, an abrupt expansion of the size of SC₂ structure is observed at $H_z \sim 10.3$, presented in (h,i). Hereafter, a zigzag spin pattern grows with decreasing H_z gradually down back to zero, with the zigzag spin pattern at $H_z = 0$ shown in (j).

spin structure upon decreasing H_z . As shown in Fig. 4(d)~(f), the simulated $\langle M_{xy} \rangle$ - H_z , $\langle M_z \rangle$ - H_z , and $\langle M_{xyz} \rangle$ - H_z curves all confirm that the zigzag spin structure with magnetization on the xy -plane develops gradually upon decreasing H_z , resulting in the nonzero total magnetization $\langle M_{xyz} \rangle$ of this spin pattern.

The above simulated results find qualitative consistency with recent experimental observations. First, the simulated $\langle \chi \rangle$ - H_z loop is in perfect agreement with measured ρ_{yx}^T - H_z loop on polycrystalline MnGe at low temperature (5 K), noting that the topological Hall resistivity ρ_{yx}^T is proportional to χ (see Fig. 2(d) in [11]). In addition, the measured $\langle M \rangle$ - H_z loop does show a linear behavior (see Fig. 4(a) in [11]), consistent with the simulated $\langle M_z \rangle$ - H_z dependence. Considering the random distribution of zigzag-patterned spin structure or SC₂ domains in the xy -plane for polycrystalline MnGe, one may compare the simulated $\langle M_z \rangle$ - H_z curves with the measured $\langle M_{xyz} \rangle$ - H_z curves. Indeed, they coincide with each other quite well.

The H_z -driven evolution from the SC₂ phase to the FM phase can be qualitatively explained, according to a theoretical formula³⁴:

$$S(x, y) = I(x, y)[M_2 \sin(qy), M_2 \cos(qx), M_1 + BM_2 \cos(qy) + BM_2 \sin(qx)]$$

$$I(x, y) = \frac{1}{\sqrt{[M_2 \sin(qy)]^2 + [M_2 \cos(qx)]^2 + [M_1 + BM_2 \cos(qy) + BM_2 \sin(qx)]^2}}, \quad (9)$$

where M_1 denotes the net magnetization induced by H_z and M_2 represents the magnetization of the SC₂ phase, factor B ($0 < B \leq 1$) again stands for the compression of the helical ordering along the z -axis induced by the easy-plane compass anisotropy.

To proceed, we separate one HSK-HASK pair into two independent primitive cells. Then, we discretize each of the HSK unit and HASK unit on a 2D mesh with up to 200×200 grids for calculating their topological winding number χ_{HSK} and χ_{HASK} , as the χ - M_z dependences plotted in Fig. 5(a). Although the field H_z is not contained explicitly in Eq. (9), we may use the χ - M_z dependence to characterize the χ - H_z dependence, by considering that H_z can be scaled by M_z as M_z increases along with H_z . We can see that the χ_{HSK} drops steeply from 0.5 to 0.0 and the χ_{HASK} from -0.5 to -1.0 with increasing M_z from 0.0 to ~ 0.2 , implying a sharp transformation from the HASK to an anti-skyrmion with $\chi = -1$ and from the HSK to a flux (vortex) state with $\chi = 0$. Consequently, a nonzero

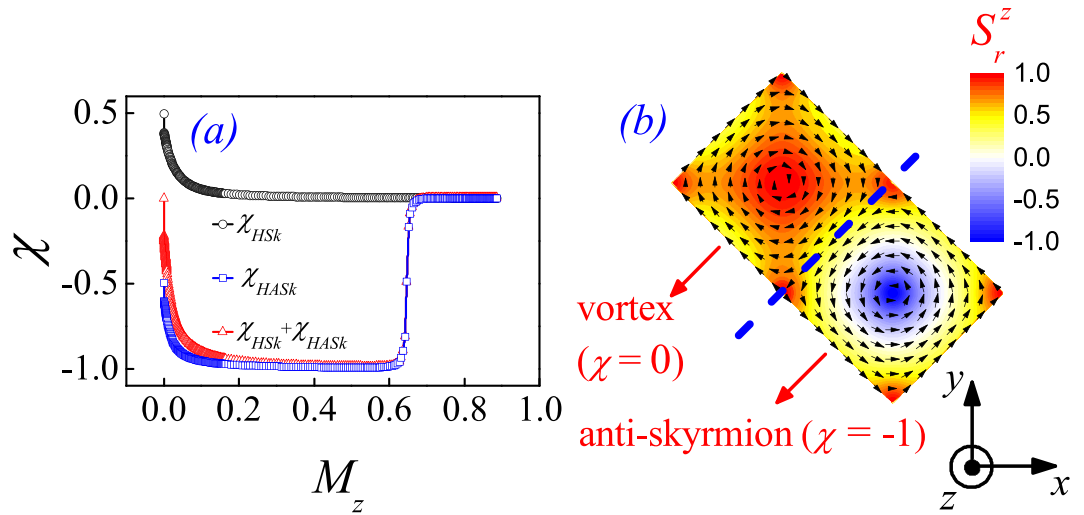


Figure 5. (a) A plot of the χ - M_z dependence for characterizing the evolution of the SC_2 phase in response to H_z , according to Eq. (9) with $B = 0.5$ chosen here. χ is counted in the region of a HSk (HASK) structure, denoted as χ_{Hsk} (χ_{HASK}). (b) A typical spin configuration at $M_z = 0.55$ is shown.

net spin chirality over the whole xy -plane emerges, as the typical spin structure at $M_z = 0.55$ shown in Fig. 5(b). Further increasing M_z from ~ 0.2 drives the SC_2 phase to deform continuously and eventually the anti-skyrmion state is melt, resulting in $\chi_{HASK} \sim 0.0$ at $M_z \sim 0.65$. The spin chirality becomes zero, corresponding to the FM phase.

To this stage, our calculations suggest the evolution sequence from the SC_2 phase to the FM phase upon increasing H_z as: (1) HASK unit \rightarrow anti-skyrmion \rightarrow flux state/vortex with zero net spin chirality \rightarrow FM state; (2) HSk unit \rightarrow flux state/vortex with zero net spin chirality \rightarrow FM state. Likewise, when H is applied along the $-z$ -axis, a transition from a HSk unit to a skyrmion is expected.

Evolution of the SC_2 phase in response to H_{-x} . As a complimentary to the last section, we also try to uncover the evolution of the SC_2 phase in response to an in-plane magnetic field, e.g. along the $-x$ -axis (H_{-x}). The main simulated results are summarized in Fig. 6. Here, we perform the MC simulation on a 64×64 lattice. Such a big size of lattice makes it better to distinguish the spin structures, and especially the periodicity of these structures. In Fig. 6(a), the simulated $\langle M_{xy} \rangle$ - H_{-x} dependence in the increasing H_{-x} sequence exhibits the multi-step magnetization. The alternating HSk and HASK crystal structure gradually decays into the FM phase with spin aligned along the $-x$ -axis, as some typical spin lattices shown in Fig. 6(d)~(h). The periodicity of the spin patterns can be measured from the Bragg intensity patterns in the upper insets, which are associated with the experimental SANS patterns¹³.

In fact, every magnetization step corresponds to a specific spin pattern. At the low- H_{-x} case, shown in Fig. 6(d), the SC_2 structure is slightly deformed from the C_4 symmetry, reflected in the two pairs of Bragg spots with different brightness. It should be noted that the experimental ring-shaped SANS pattern, formed in the polycrystalline powder, is generated by the randomly oriented multiple- q structures with the same magnitude of magnetic modulation vector (see Fig. 3(a) in [13]). Therefore, the ring pattern is associated with the formation of a periodically modulated magnetic structure (i.e., the SC_2 phase here). Further increasing H_{-x} triggers some stripe-like domains along the x -axis shown in Fig. 6(e) at $H_{-x} = 0.35$. These stripes are mixture of the alternating HSk and HASK crystal structure and the FM state aligned along the $-x$ -axis with inharmonic periodicity. The corresponding Bragg intensity pattern shows a pair of Bragg spots in the q_x -axis and two pairs of Bragg spots in the q_y -axis, in good agreement with the crescent-shaped SANS pattern observed experimentally (Fig. 3(b) in [13]). At very high H_{-x} , the Bragg spots shrink and the lattice gradually gives away to the FM phase, also consistent with experiments¹³. Similar features can be found in the $\langle \gamma \rangle$ - H_{-x} curve (Fig. 6(b)). When H_{-x} is gradually ramped down back to zero, a spiral state emerges at $H_{-x} \sim 0.3$. As shown in Fig. 6(i), the spiral propagates along the $-x$ -axis with a good periodicity, as the variation in the Bragg patterns again shows good consistence with the variation of SANS patterns (see Fig. 3(e)~(h) in [13]).

It is noted from the $\langle E \rangle$ - H_{-x} curves in Fig. 6(c) that, the spiral state is degenerate with the alternating HSk and HASK crystal structure at $H_{-x} = 0$. However, energy of the states formed in the process of increasing H_{-x} is apparently higher than that in the process of decreasing H_{-x} at the range of $0 < H_{-x} < \sim 1.8$. In this regard, we reckon that the alternating HSk and HASK crystal structure is a strongly frustrated spin system³⁹. This is why the multi-step magnetization appearing in the $\langle M_{xy} \rangle$ - H_{-x} curve in Fig. 6(a).

Discussions

Before concluding this work, we briefly discuss experimental realization of the SC_2 phase. B20-type helimagnets with another type of easy-plane anisotropy $A_s(S_i^z)^2$ ($A_s > 0$) were also studied by MC simulation, which shows that this anisotropy may lead to the alternating HSk and HASK crystal structures on a square lattice at proper A too⁴⁰. In addition, skyrmions in B20-type helimagnet thin films with easy-plane anisotropy $A_s(S_i^z)^2$ ($A_s > 0$) were recently studied using a micromagnetic model including demagnetization and a three-dimensional geometry⁴¹.

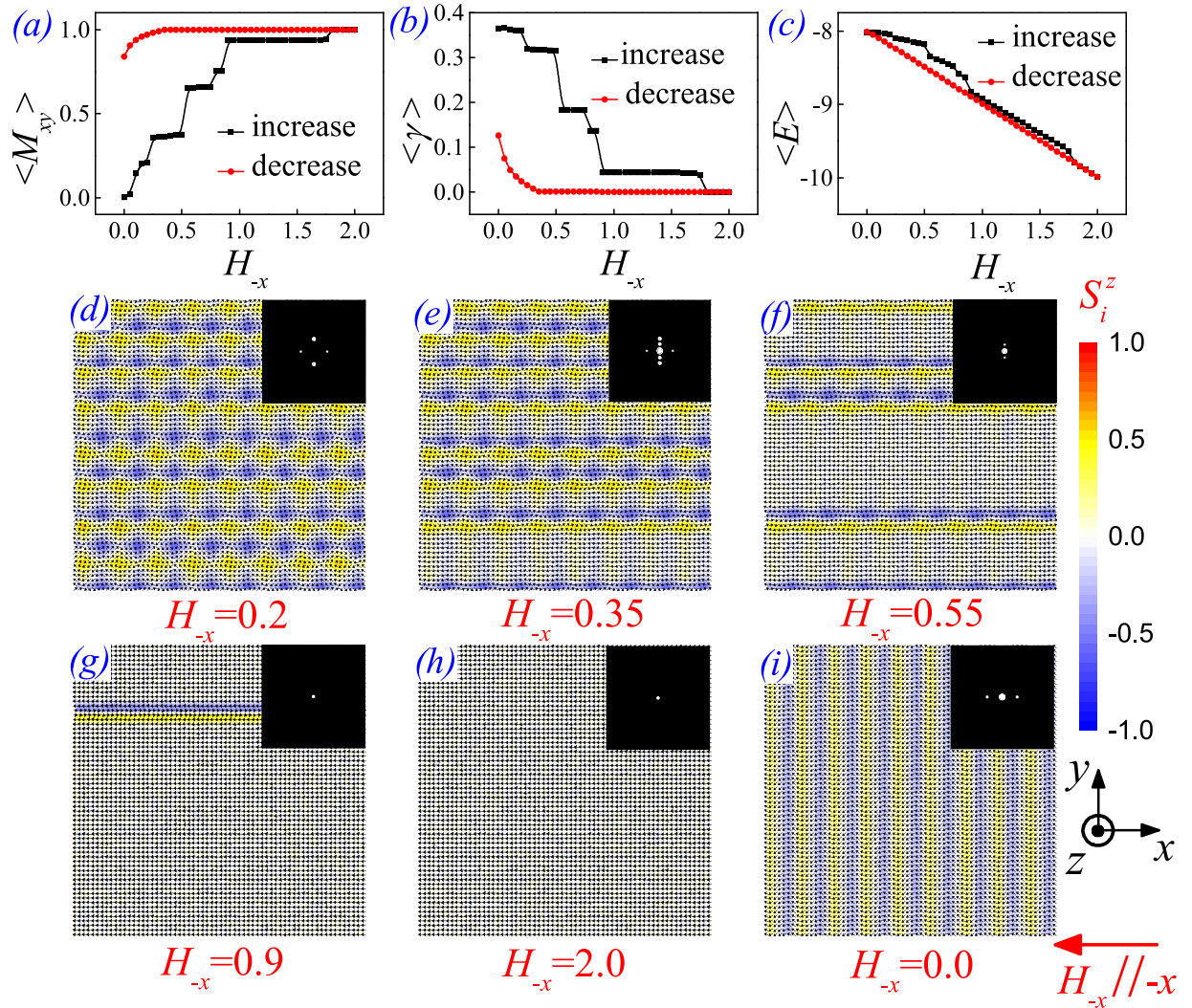


Figure 6. Plots of various physical quantities as a function of H_{-x} : (a) $\langle M_{xy} \rangle$, (b) $\langle \gamma \rangle$, and (c) energy per spin $\langle E \rangle$. In this process, spin configuration evolves from the initial SC_2 state at $H = 0$ to a saturated FM phase driven by the increasing H_{-x} , with some typical states shown in (d)~(h). Hereafter, a spiral spin pattern grows upon decreasing H_{-x} gradually down back to zero, with the spiral state at $H_{-x} = 0$ shown in (i). The upper insets in (d)~(i) are the corresponding Bragg intensity $|S(q)|^2$ patterns for each spin configuration.

This work showed the demagnetization effects and/or the finite thickness effects on the skyrmion energetics and stability, which were explicitly demonstrated in earlier studies^{42,43}. Therefore, B20-type helimagnet thin films seem to be appropriate for realizing the SC_2 phase, because the uniaxial anisotropy (A_z), compass anisotropy (A_c) as well as the demagnetization can be altered significantly by varying the film thickness and the laterally confined geometries^{27,41–42,44}. Furthermore, hedgehog skyrmions in chiral magnets with Rashba SOC were previously studied by variational energy calculations, which imposes a topological constraint for the center and boundary spins in a unit cell¹⁶. This constraint allows the hedgehog skyrmions but naturally exclude the HSK or HASK states in the chiral magnets. Therefore, whether the compass anisotropy can lead to the energetically stable HSK or HASK states in chiral magnets with Rashba SOC is yet to be explored.

On the other hand, temperature dependence of the Hall resistivity, susceptibility and magnetic modulation vector in MnGe was revealed by experiments^{11,13}. These features are also important for our understanding of the underlying physics of MnGe, which would be an interesting challenge for our further studies.

In summary, we have presented in this work a detailed analysis of a classical microscopic spin model comprising FM exchange, DM interaction, compass anisotropy, and Zeeman energy, which may be widely used for the chiral magnets with strong SOC. We use classical MC simulation to determine the low temperature phase diagram as a function of compass anisotropy and out-of-plane magnetic field. In this phase diagram, we propose the alternating HSK and HASK crystal structures on a square lattice to be the candidate for the zero-field ground state of the helimagnet MnGe. The simulated evolution of the spin structure driven by magnetic field is in good accordance with experimental observations on MnGe. Therefore, our microscopic spin model successfully captures the main physics responsible for the magnetic structures in the helimagnet MnGe. This study may also

provide a new theoretical guide to understand the magnetic states in other systems (such as the complex oxide heterostructure interfaces, and artificial ultracold Bose gas) with strong SOC, and may bring some insights for the future experiments.

Methods

Simulation algorithm. In this work, we perform MC simulations based on the standard single-flip Metropolis algorithm combined with the over-relaxation method. This clustering algorithm is believed to be effective in equilibrating the frustrated spin models with a large size^{45–47}. Our unit MC step consists of one Metropolis sweep and ten over-relaxation sweeps. Most calculations are carried out on a 32×32 lattice with periodic boundary conditions, and then further checked on a lattice with bigger size of 64×64 , in which case the simulation results remain the same. For reaching the ground state, an annealing simulation scheme is employed. First, a paramagnetic lattice is chosen as the initial lattice and each simulation cycle starts from sufficiently high temperature (T). Then the lattice is cooled down gradually until a very low $T = 0.01$ ^{8,31}. The as-obtained spin state is treated approximately as the ground state.

For tracking the evolution of non-zero field spin states, a ladder protocol following earlier reports^{39,48,49} is employed. The corresponding zero-field ground state is chosen as the initial lattice, and then magnetic field H is varied following the linear protocol $H(j) = H(j-1) + \delta t$, where $H(j)$ ($j = 1, 2, 3, \dots$) is the field at stage j , δ is a constant, and t is time measured in MC steps. In the protocol, the lattice at $H(j-1)$ is taken as the initial lattice for calculating the state at $H(j)$. Besides, we discard the data in the first N_e MC steps needed for equilibration, and calculate the averages over the following N_c MC steps at every $H(j)$ stage. Typically, both N_e and N_c are 5×10^5 . During this procedure, field H is increased from $H = 0$ till a sufficiently big magnitude so that the lattice reaches the field-driven FM state. Subsequently, the field is reduced back to $H = 0$ for exploring potential hysteresis behavior if any.

References

- Qi, X. L. & Zhang, S. C. The quantum spin Hall effect and topological insulators. *Phys. Today* **63**, 33–38 (2010).
- Hasan, M. Z. & Kane, C. L. Colloquium: topological insulators. *Rev. Mod. Phys.* **82**, 3045 (2010).
- Ishikawa, Y., Tajima, K., Bloch, D. & Roth, M. Helical spin structure in manganese silicide MnSi. *Solid State Commun.* **19**, 525–528 (1976).
- Mühlbauer, S. *et al.* Skyrmion lattice in a chiral magnet. *Science* **323**, 915–919 (2009).
- Bak, P. & Jensen, M. H. Theory of helical magnetic structures and phase transitions in MnSi and FeGe. *J. Phys. C: Solid State Phys.* **13**, L881 (1980).
- Yu, X. Z. *et al.* Near room-temperature formation of a skyrmion crystal in thin-films of the helimagnet FeGe. *Nat. Mater.* **10**, 106–109 (2011).
- Beille, J., Voiron, J. & Roth, M. Long period helimagnetism in the cubic B20 $\text{Fe}_x\text{Co}_{1-x}\text{Si}$ and $\text{Co}_x\text{Mn}_{1-x}\text{Si}$ alloys. *Solid State Commun.* **47**, 399–402 (1983).
- Yu, X. Z. *et al.* Real-space observation of a two-dimensional skyrmion crystal. *Nature* **465**, 901–904 (2010).
- Seki, S., Yu, X. Z., Ishiwata, S. & Tokura, Y. Observation of skyrmions in a multiferroic material. *Science* **336**, 198–201 (2012).
- Nagaosa, N. & Tokura, Y. Topological properties and dynamics of magnetic skyrmions. *Nat. Nanotech.* **8**, 899–911 (2013).
- Kanazawa, N. *et al.* Large topological Hall effect in a short-period helimagnet MnGe. *Phys. Rev. Lett.* **106**, 156603 (2011).
- Neubauer, A. *et al.* Topological Hall effect in the A phase of MnSi. *Phys. Rev. Lett.* **102**, 186602 (2009).
- Kanazawa, N. *et al.* Possible skyrmion-lattice ground state in the B20 chiral-lattice magnet MnGe as seen via small-angle neutron scattering. *Phys. Rev. B* **86**, 134425 (2012).
- Stishov, S. M. & Petrova, A. E. Itinerant helimagnet MnSi. *Phys.-Usp.* **54**, 1117–1130 (2011).
- Banerjee, S., Erten, O. & Randeria, M. Ferromagnetic exchange, spin-orbit coupling and spiral magnetism at the $\text{LaAlO}_3/\text{SrTiO}_3$ interface. *Nat. Phys.* **9**, 626–630 (2013).
- Banerjee, S., Rowland, J., Erten, O. & Randeria, M. Enhanced stability of skyrmions in two-dimensional chiral magnets with Rashba spin-orbit coupling. *Phys. Rev. X* **4**, 031045 (2014).
- Cole, W. S., Zhang, S., Paramekanti, A. & Trivedi, N. Bose-Hubbard models with synthetic spin-orbit coupling: Mott insulators, spin textures, and superfluidity. *Phys. Rev. Lett.* **109**, 085302 (2012).
- Zhang, D. W., Chen, J. P., Shan, C. J., Wang, Z. D. & Zhu, S. L. Superfluid and magnetic states of an ultracold Bose gas with synthetic three-dimensional spin-orbit coupling in an optical lattice. *Phys. Rev. A* **88**, 013612 (2013).
- Farrell, A. & Pereg-Barnea, T. Strong coupling expansion of the extended Hubbard model with spin-orbit coupling. *Phys. Rev. B* **89**, 035112 (2014).
- Nussinov, Z. & van den Brink, J. Compass models: Theory and physical motivations. *Rev. Mod. Phys.* **87**, 1 (2015).
- van den Brink, J. Orbital-only models: ordering and excitations. *New J. Phys.* **6**, 201 (2004).
- Jackeli, G. & Khaliullin, G. Mott insulators in the strong spin-orbit coupling limit: from Heisenberg to a quantum compass and Kitaev models. *Phys. Rev. Lett.* **102**, 017205 (2009).
- Yildirim, T., Harris, A. B., Entin-Wohlman, O. & Aharony, A. Symmetry, spin-orbit interactions, and spin anisotropies. *Phys. Rev. Lett.* **73**, 2919 (1994).
- Bert, J. A. *et al.* Direct imaging of the coexistence of ferromagnetism and superconductivity at the $\text{LaAlO}_3/\text{SrTiO}_3$ interface. *Nat. Phys.* **7**, 767–771 (2011).
- Caviglia, A. D. *et al.* Tunable Rashba spin-orbit interaction at oxide interfaces. *Phys. Rev. Lett.* **104**, 126803 (2010).
- Butenko, A. B., Leonov, A. A., Röbller, U. K. & Bogdanov, A. N. Stabilization of skyrmion textures by uniaxial distortions in noncentrosymmetric cubic helimagnets. *Phys. Rev. B* **82**, 052403 (2010).
- Johnson, M. T., Bloemen, P. J. H., den Broeder, F. J. A. & de Vries, J. J. Magnetic anisotropy in metallic multilayers. *Rep. Prog. Phys.* **59**, 1409 (1996).
- King, P. D. C. *et al.* Large tunable Rashba spin splitting of a two-dimensional electron gas in Bi_2Se_3 . *Phys. Rev. Lett.* **107**, 096802 (2011).
- Li, X., Liu, W. V. & Balents, L. Spirals and skyrmions in two dimensional oxide heterostructures. *Phys. Rev. Lett.* **112**, 067202 (2014).
- Landau, D. P. & Binder, K. In *A Guide to Monte Carlo Simulations in Statistical Physics* 2nd edn, 68–190 (Cambridge, 2008).
- Yi, S. D., Onoda, S., Nagaosa, N. & Han, J. H. Skyrmions and anomalous Hall effect in a Dzyaloshinskii-Moriya spiral magnet. *Phys. Rev. B* **80**, 054416 (2009).
- Makarova, O. L. *et al.* Neutron diffraction study of the chiral magnet MnGe. *Phys. Rev. B* **85**, 205205 (2012).
- Shibata, K. *et al.* Towards control of the size and helicity of skyrmions in helimagnetic alloys by spin-orbit coupling. *Nat. Nanotech.* **8**, 723–728 (2013).
- Binz, B. & Vishwanath, A. Chirality induced anomalous-Hall effect in helical spin crystals. *Physica B* **403**, 1336–1340 (2008).

35. Park, J.-H. & Han, J. H. Zero-temperature phases for chiral magnets in three dimensions. *Phys. Rev. B* **83**, 184406 (2011).
36. Lee, S. Y. & Han, J. H. Zero-energy bound states in a nodal topological lattice. *Phys. Rev. B* **91**, 245121 (2015).
37. Alba, E., Fernandez-Gonzalvo, X., Mur-Petit, J., Pachos, J. K. & Garcia-Ripoll, J. J. Seeing topological order in time-of-flight measurements. *Phys. Rev. Lett.* **107**, 235301 (2011).
38. Pfleiderer, C. Magnetic order: Surfaces get hairy. *Nat. Phys.* **7**, 673–674 (2011).
39. Chen, J. P. *et al.* Manipulation of magnetic state in nanostructures by perpendicular anisotropy and magnetic field. *J. Appl. Phys.* **115**, 243910 (2014).
40. Lin, S. Z., Saxena, A. & Batista, C. D. Skyrmion fractionalization and merons in chiral magnets with easy-plane anisotropy. *Phys. Rev. B* **91**, 224407 (2015).
41. Vousden, M. *et al.* Skyrmions in thin films with easy-plane magnetocrystalline anisotropy. *Appl. Phys. Lett.* **108**, 132406 (2016).
42. Beg, M. *et al.* Ground state search, hysteretic behaviour, and reversal mechanism of skyrmionic textures in confined helimagnetic nanostructures. *Sci. Rep.* **5**, 17137 (2015).
43. Rybakov, F. N., Borisov, A. B. & Bogdanov, A. N. Three-dimensional skyrmion states in thin films of cubic helimagnets. *Phys. Rev. B* **87**, 094424 (2013).
44. Karhu, E. A. *et al.* Chiral modulations and reorientation effects in MnSi thin films. *Phys. Rev. B* **85**, 094429 (2012).
45. Creutz, M. Overrelaxation and Monte Carlo simulation. *Phys. Rev. D* **36**, 515 (1987).
46. Campos, I., Cotallo-Aban, M., Martin-Mayor, V., Perez-Gaviro, S. & Tarancon, A. Spin-glass transition of the three-dimensional Heisenberg spin glass. *Phys. Rev. Lett.* **97**, 217204 (2006).
47. Viet, D. X. & Kawamura, H. Numerical evidence of spin-chirality decoupling in the three-dimensional Heisenberg spin glass model. *Phys. Rev. Lett.* **102**, 027202 (2009).
48. Carubelli, M. *et al.* Spin reorientation transition and phase diagram of ultrathin ferromagnetic films. *Phys. Rev. B* **77**, 134417 (2008).
49. Chen, J. P. *et al.* Stripe-vortex transitions in ultrathin magnetic nanostructures. *J. Appl. Phys.* **113**, 054312 (2013).

Acknowledgements

We thank P. Chu for stimulating discussions. This work was supported by the National Key Research Programme of China (Grant No. 2016YFA0300101), the Natural Science Foundation of China (11234005 and 11374147), the Priority Academic Program Development of Jiangsu Higher Education Institutions, China, the Foundation for Fostering the Scientific and Technical Innovation of Guangzhou University, the Science Research Foundation for Young Teachers in South China Normal University (15KJ16), and the Foundation for Distinguished Young Talents in Higher Education of Guangdong (2015KQNCX023).

Author Contributions

J.M.L. conceived the research project and J.P.C. performed the computations. J.P.C., D.W.Z., and J.M.L. commented the modeling and discussed the results. J.P.C. and J.M.L. wrote the paper.

Additional Information

Competing financial interests: The authors declare no competing financial interests.

How to cite this article: Chen, J. P. *et al.* Exotic skyrmion crystals in chiral magnets with compass anisotropy. *Sci. Rep.* **6**, 29126; doi: 10.1038/srep29126 (2016).



This work is licensed under a Creative Commons Attribution 4.0 International License. The images or other third party material in this article are included in the article's Creative Commons license, unless indicated otherwise in the credit line; if the material is not included under the Creative Commons license, users will need to obtain permission from the license holder to reproduce the material. To view a copy of this license, visit <http://creativecommons.org/licenses/by/4.0/>